

Progress in Modeling 3D Shear Flows Using RANS Equations and Advanced Turbulence Models

Fotis Sotiropoulos

School of Civil and Environmental Engineering

Georgia Institute of Technology

Atlanta, Georgia 30332-0355, USA

Email: fsotirop@ce.gatech.edu

Abstract

This article reviews recent work in the area of advanced turbulence modeling for complex three-dimensional flows of engineering interest. The term “advanced” refers herein to models that resolve the near-wall flow and account for the anisotropy of the Reynolds stresses. Representative such models, including full Reynolds-stress transport and non-linear, two-equation models, that have already been successfully applied to complex flows are presented and their advantages and inherent limitations are discussed. Critical numerical issues that need to be addressed in order to facilitate the application of such models to complex flows are also examined. Emphasis is placed on high-resolution spatial discretization schemes and strongly coupled multigrid acceleration strategies for efficient and robust solution algorithms on stretched, large-aspect-ratio grids. Examples from applications of advanced turbulence models to three-dimensional flows are presented. The test cases considered include both internal and external flows with strong longitudinal vortices. Comparisons of the computed results with available experimental data point to the conclusion that quantitatively accurate predictions of complex shear flows require turbulence models that resolve the near-wall flow and account for turbulence anisotropy. The implications of these findings for future predictions of complex engineering flows are discussed.

1 Introduction

In spite of rapid advancements in computational power and significant strides in numerical algorithm development, the prediction of complex, three-dimensional shear flows continues to pose a grand challenge for computational fluid dynamics (CFD). Such flows take place at high Reynolds numbers in and around shapes of arbitrary geometrical complexity. They are typically characterized by strong surface curvatures, induced pressure gradients, three-dimensional separation and vortex formation, large-scale unsteadiness, surface roughness, etc. These complicating effects, which in most real-life flows co-exist simultaneously, give rise to turbulence fields that cannot be described by models relying on the simplistic assumptions of local equilibrium and turbulence isotropy.

The direct numerical simulation (DNS) approach, which has yielded important insights into the structure of relatively simple, low Reynolds number flows, cannot be used to predict engineering flows, at least not within the foreseeable future. DNS will instead continue to provide important databases of instantaneous turbulence fields that will guide refinement and new development of simpler engineering calculation models. The more realistic, from a computational standpoint, large-eddy simulation (LES) approach, which has attracted considerable attention during the past decade, has not in general lived up to initial expectations [1]. Although encouraging results for complex flows at moderate Reynolds numbers have been reported in the literature [2,3], meaningful LES at Reynolds numbers of engineering interest would still require grid resolutions that are beyond the capabilities of existing and projected computer capacity. This state of affairs leaves methods that rely on the Reynolds-averaged Navier–Stokes (RANS) equations as the most promising alternative for practical engineering computations. During the past decade such methods were successfully employed, in conjunction with near-wall, non-isotropic turbulence closures, to simulate complex, three-dimensional flows with vortices [4 – 8]. Although discrepancies between predictions and experiments still remain, these studies succeeded, for the first time, in resolving complex features of both the mean flow and turbulence fields, which simple isotropic turbulence models had failed to describe even in a gross qualitative sense.

The success of these advanced RANS simulations, coupled with the continuous improvements in Reynolds-stress turbulence models and the advancements in computational power, have stimulated new ideas for predicting complex turbulent flows. Speziale [1] recently proposed a framework that allows a DNS to go continuously to an unsteady RANS simulation through LES and very large eddy simulations (VLES), depending on the grid resolution. A critical prerequisite for establishing such an approach as a practical predictive tool is, according to Speziale [1], to take advantage of and further build upon the success of state-of-the-art, non-isotropic turbulence closures for the RANS equations. We anticipate such ideas, which combine advanced unsteady RANS models with LES and VLES formulations, to attract increasing attention within the coming years in the CFD's community quest toward predictive methods for real-life flows.

In this article, we seek to: summarize the experience gained from recent applications of advanced RANS methods to steady in the mean turbulent flows; emphasize both the successes and failures of these studies; and underscore the issues that need to be addressed before such methods can be extended to develop the next generation of unsteady RANS/VLES models. We should clarify that our goal herein is not to provide a complete review of advanced turbulence models (for reviews see [1, 9, 10]). Instead, we will focus on a few select models that have been successfully applied to simulate three-dimensional, incompressible turbulent flows [4 – 8]. The models we will discuss include the full Reynolds-stress transport models of Gibson and Launder (GL) [11] and Launder and Shima (LSH) [12, 13], non-linear two equations models based on quadratic [14] and cubic [15] constitutive relations, as well as some standard isotropic, two-equation models [16, 17]. The relative performance of these models will be gauged by reviewing results of their applications to internal and external, complex, three-dimensional shear flows. We will also review our recent work in the area of numerical algorithms for complex, turbulent flows [18, 19], as there are a number of challenging numerical issues that need to be addressed before advanced turbulence models can be adopted as engineering calculation tools. Special emphasis will be placed on strongly coupled, multigrid strategies—which apply multigrid acceleration simultaneously to the mean flow and turbulence closure equations—that have shown promise

in alleviating numerical stiffness on stretched computational meshes. The role of spatial discretization schemes on the accuracy of the computed solutions will also be discussed in detail.

The article is organized as follows. In Section 2 we present the RANS equations and various turbulence closures formulated in generalized curvilinear coordinates. In Section 3 we describe and evaluate the performance of a strongly coupled, multigrid, finite-volume algorithm for solving the RANS equations in complex geometries. In Section 4 we review applications of various advanced turbulence models to internal and external complex shear flows. Finally, in Section 5 we summarize our findings and draw conclusions about future research directions.

2 The governing equations

2.1 Mean Flow Equations

The three-dimensional, incompressible, RANS equations, non-dimensionalized by the fluid density ρ , reference velocity U_o , and reference length L_o , are formulated in strong conservation form and transformed in curvilinear coordinates (ξ^1, ξ^2, ξ^3) . The transformed RANS equations read in compact tensor notation, where repeated indices imply summation, as follows:

$$\Gamma \frac{1}{J} \frac{\partial Q_f}{\partial t} + \frac{\partial}{\partial \xi^j} (F_f^j - F_{f_{rs}}^j - F_{f_v}^j) = 0 \quad (1)$$

where J is the Jacobian of the geometric transformation, $\Gamma = \text{diag}(0, 1, 1, 1)$, and the vectors in eqn. (1) are defined as follows:

$$Q_f = [p, U_1, U_2, U_3]^T \quad (2)$$

$$F_f^j = \frac{1}{J} [V^j, U_1 V^j + p \xi_{x_1}^j, U_2 V^j + p \xi_{x_2}^j, U_3 V^j + p \xi_{x_3}^j]^T \quad (3)$$

$$F_{f_{rs}}^j = \frac{1}{J} \left[0, -\xi_{x_j}^\ell \overline{u_1 u_\ell}, -\xi_{x_j}^\ell \overline{u_2 u_\ell}, -\xi_{x_j}^\ell \overline{u_3 u_\ell} \right]^T \quad (4)$$

$$F_{f_v}^j = \frac{1}{J} \frac{1}{\text{Re}} g^{mj} \frac{\partial}{\partial \xi^m} (\Gamma Q_f) \quad (5)$$

In the above equations, p is the static pressure, U_i are the mean Cartesian velocity components, $-\rho \overline{u_i u_j}$ are the components of the Reynolds-stress tensor, $\xi_{x_j}^i$ are the metrics of the geometric transformation, V^j are the contravariant velocity components ($V^j = U_i \xi_{x_i}^j$), and g^{ij} are the components of the contravariant metric tensor ($g^{ij} = \xi_{x_k}^i \xi_{x_k}^j$). Finally, Re is the Reynolds number ($Re = U_o L_o / \nu$).

2.2 Turbulence Closure Equations

Closure of eqn. (1) requires modeling the components of the Reynolds-stress tensor in terms of mean flow quantities. We describe herein several such models, which we have employed in computations of complex, three-dimensional flows. These include, differential Reynolds-stress transport models (or second-moment closures), non-linear (or non-isotropic), eddy-viscosity, two-equation models, and standard, isotropic, two-equation models. The various models can be formulated, in a unified manner, in flux-vector form as follows:

$$\frac{1}{J} \frac{\partial Q_t}{\partial t} + \frac{\partial}{\partial \xi^j} (F_t^j - F_{t_v}^j - F_{t_r}^j) - H_t = 0 \quad (6)$$

where the various vectors are defined for each model in the subsequent sections.

2.2.1 Second-moment closures

Second-moment closures, or Reynolds-stress transport models, solve transport equations for the six components of the Reynolds stress tensor and the rate of energy dissipation ϵ . They comprise, therefore, the most

advanced level of turbulence modeling within the RANS framework. We describe here two such models: (i) the GL high Reynolds number model [11]; and (ii) the near-wall version of the GL model originally proposed by Launder and Shima [12] (LSH) and later modified by Shima [13]. Due to space considerations, only a general outline of the model equations is given below. For detailed equations the reader is referred to the original papers [11 – 13].

For the GL and LSH closures the various terms in eqn. (6) are defined as follows:

$$Q_t = [\overline{u_1^2} \quad \overline{u_2^2} \quad \overline{u_3^2} \quad \overline{u_1 u_2} \quad \overline{u_1 u_3} \quad \overline{u_2 u_3} \quad \varepsilon]^T; \quad (7a)$$

convective fluxes

$$F_t^j = \frac{V^j}{J} Q_t; \quad (7b)$$

viscous diffusion fluxes

$$F_{t_v}^j = \frac{g^{mj}}{J \text{Re}} \frac{\partial}{\partial \xi^m} (Q_t); \quad (7c)$$

turbulent diffusion fluxes

$$F_{t_r}^j = \frac{1}{J} [d_{11}^j \quad d_{22}^j \quad d_{33}^j \quad d_{12}^j \quad d_{13}^j \quad d_{23}^j \quad d_\varepsilon^j]^T, \quad (7d)$$

$$d_{pq}^j = C_s \frac{k}{\varepsilon} \xi_{x_\ell}^m \xi_{x_n}^j \left(\overline{u_p u_\ell} \frac{\partial \overline{u_q u_n}}{\partial \xi^m} + \overline{u_q u_\ell} \frac{\partial \overline{u_n u_p}}{\partial \xi^m} + \overline{u_n u_\ell} \frac{\partial \overline{u_p u_q}}{\partial \xi^m} \right),$$

$$d_\varepsilon^j = C_\varepsilon \frac{k}{\varepsilon} \xi_{x_\ell}^m \xi_{x_n}^j \overline{u_\ell u_n} \frac{\partial \varepsilon}{\partial \xi^m};$$

source terms

$$H_t = \frac{1}{J} \left[h_{11}, h_{22}, h_{33}, h_{13}, h_{12}, h_{23}, (C_{\varepsilon_1} + \psi_1 + \psi_2) \frac{\varepsilon}{k} P - C_{\varepsilon_2} \frac{\varepsilon \tilde{\varepsilon}}{k} \right]^T, \quad (7e)$$

$$h_{ij} = P_{ij} - \frac{2}{3} \varepsilon \delta_{ij} + \Phi_{ij},$$

where P_{ij} is the production of the Reynolds stresses by mean shear,

$$P_{ij} = - \left(\overline{u_i u_k} \frac{\partial U_j}{\partial \xi^\ell} \xi_{x_k}^\ell + \overline{u_j u_k} \frac{\partial U_i}{\partial \xi^\ell} \xi_{x_k}^\ell \right), \quad (7f)$$

and Φ_{ij} is the pressure-strain (or pressure-redistribution) correlation tensor, modeled as

$$\begin{aligned} \Phi_{ij} &= -C_1 \varepsilon \left(\frac{\overline{u_i u_j}}{k} - \frac{2}{3} \delta_{ij} \right) - C_2 \left(P_{ij} - \frac{2}{3} P \delta_{ij} \right) + \Phi_{ij_1}^w + \Phi_{ij_2}^w, \quad (7g) \\ \Phi_{ij_1}^w &= C_1^w \frac{\varepsilon}{k} \left(\overline{u_p u_q} n_p n_q \delta_{ij} - \frac{3}{2} \overline{u_p u_i} n_p n_j - \frac{3}{2} \overline{u_p u_j} n_p n_i \right) f, \\ \Phi_{ij_2}^w &= C_2^w \left(\Phi_{pq_2} n_p n_q \delta_{ij} - \frac{3}{2} \Phi_{ip_2} n_p n_j - \frac{3}{2} \Phi_{jp_2} n_p n_i \right) f. \end{aligned}$$

In the above equations, n_i is the i th component of the unit vector perpendicular to the wall, which for a wall located at $\xi^3=0$ is given by $n_i = \xi_{x_i}^3 / \sqrt{g^{33}}$, P is the production of turbulence kinetic energy ($P = P_{kk}/2$), and f is a near-wall damping function that depends on the normal distance from the nearest wall [11].

For the high-Reynolds number model of GL, the coefficients C_1 , C_2 , C_1^w , C_2^w , $C_{\varepsilon 1}$, and $C_{\varepsilon 2}$ are constants [11], $\psi_1 = \psi_2 = 0$, and $\varepsilon = \varepsilon$. Boundary conditions for the GL model are obtained by employing the three-point wall functions approach developed by Sotiropoulos and Patel [6]. To facilitate the description of this procedure, assume that the wall is located at $\xi^k=0$. When constructing the computational mesh we ensure that the three near-wall coordinate surfaces $\xi^k=1, 2$, and 3 are located within the fully turbulent region (typically in the range $70 < n^+ < 100$, where $n^+ = u_\tau n / \nu$, u_τ is the friction velocity, $u_\tau = \sqrt{\tau_w / \rho}$, and n is the normal distance from the wall). Starting now from an appropriate initial guess, the momentum, Reynolds-stress and ε equations are advanced to the next time level up to the $\xi^k=3$ surface. The magnitude of the computed velocity vector at $\xi^k=3$ is then used in conjunction with the logarithmic law-of-the-wall to obtain the friction

velocity u_τ —the resulting non-linear equation is solved with the Newton-Raphson method. With u_τ known, the law of the wall is once again employed to obtain the magnitude of the velocity vectors at $\xi^k=1$ and 2. The three Cartesian velocity components at $\xi^k=1$ and 2 can then be computed by: (i) assuming that the flow is parallel to the wall, and (ii) obtaining the angle between the streamwise coordinate and the projection of the velocity vector on the wall via extrapolation from the interior nodes. The velocity components at $\xi^k=2$ serve as boundary conditions for the momentum equations, while those at $\xi^k=1$ are used to discretize, at $\xi^k=2$, the velocity gradient terms in the production and pressure-strain tensors that appear in the modeled Reynolds-stress equations. The Reynolds stresses at $\xi^k=2$, necessary for computing the Reynolds-stress gradients in the momentum equations and for providing boundary conditions for the Reynolds-stress transport equations at $\xi^k=3$, are obtained in accordance with a local equilibrium assumption by setting all transport terms in the GL closure equal to zero and solving the resulting system of algebraic equations. The energy dissipation at $\xi^k=2$ is obtained by setting it equal to the production of turbulence kinetic energy.

For the near-wall version of the model (LSH), the coefficients C_1 , C_2 , C_1^w , and C_2^w are functions of the second and third invariants of the anisotropy tensor and the turbulence Reynolds number to account for departures from local isotropy and guarantee that the various structural parameters approach correct asymptotic limits in the vicinity of the wall [12, 13]. The ψ_1 and ψ_2 terms in the ε -equation are functions of P/ε , the invariants of the anisotropy tensor, and the turbulence Reynolds number. They were introduced by Launder and Shima [12] and more recently modified by Shima [13] to produce the proper length scales in boundary layers in pressure gradients. Finally, $\tilde{\varepsilon}$ is defined, for a wall located at $\xi^3 = \text{const.}$, as follows:

$$\tilde{\varepsilon} = \varepsilon - 2\nu \left(g^{i3} \frac{\partial \sqrt{k}}{\partial \xi^i} \right)^2.$$

On solid walls, the components of the Reynolds-stress tensor are set equal to zero, whereas ε is computed by setting $\tilde{\varepsilon} = 0$.

The applicability of both the GL and LSH closures to complex geometries with multiple intersecting walls is hindered considerably by the presence of the wall orientation (wall normal vectors n_k) and proximity (f function in the pressure-strain model) parameters (eqn. (7g)). In the applications reviewed below, we have avoided such problems by considering geometrical configurations that, by appropriate selection of curvilinear coordinates, can be discretized with mesh topologies in which the solid surface coincides with a single coordinate surface. Of course, this cannot always be accomplished in general, three-dimensional domains. Some remedies have been proposed in the literature to account for the effects of multiple walls by defining generalized distance functions and linearly superimposing the effects of individual walls [20]. These, however, are rather *ad-hoc* engineering approximations and lack rigor and generality. It is for these reasons, that there have been considerable efforts devoted to developing second-moment closures that do not contain wall orientation and proximity parameters [21 – 24]. Although promising results have been obtained for two-dimensional flows [24], the performance of such approaches in complex, three-dimensional shear flows remains to be evaluated.

2.2.2 Two-equation, eddy-viscosity models

Two-equation models rely on the eddy-viscosity, ν_t , concept to express the components of the Reynolds-stress tensor in terms of the mean velocity gradients via algebraic constitutive laws. Based on the order of the constitutive equation employed, such models are classified as linear (or isotropic) or non-linear closures.

Linear eddy-viscosity models are widely used in engineering computations today and, as implied by their name, assume a linear relation between the Reynolds-stress and mean rate-of-strain tensors:

$$\overline{-u_i u_j} = -\frac{2}{3} k \delta_{ij} + \nu_t S_{ij}, \quad (8)$$

where S_{ij} is the mean rate-of-strain tensor, given by

$$S_{ij} = \xi_{x_j}^k \frac{\partial U_i}{\partial \xi^k} + \xi_{x_i}^k \frac{\partial U_j}{\partial \xi^k}.$$

The above linear law yields isotropic normal Reynolds stresses in fully developed turbulent flow through straight non-circular ducts. It thus fails to predict Prandtl's secondary currents of the second kind (also known as stress-driven secondary motion), which are driven by the anisotropy of the Reynolds stresses.

Non-linear constitutive laws employ higher-order functional relations to express the Reynolds-stress tensor in terms of both the mean rate-of-strain and rotation tensors. Several such relations have been proposed in the literature [14, 15, 25, 26] and received considerable attention as they provide a cost-effective alternative to full second-moment closures. Unlike the linear constitutive law of eqn. (8), such models can predict, at least in a qualitative sense, stress-driven secondary currents as they produce anisotropic normal stresses even in straight non-circular ducts [25]. We present here two such relations, which we have employed to calculate three-dimensional shear flows. The first is the quadratic constitutive equation proposed by Gatski and Speziale [14] (denoted hereafter as GS):

$$\overline{u_i u_j} = \frac{2}{3} k \delta_{ij} - 2v_t \left[\frac{1}{2} S_{ij} + \frac{\ell_t}{4u_t} \left(\alpha_4 (S_{ik} \Omega_{kj} - S_{jk} \Omega_{ki}) - \alpha_5 (S_{ik} S_{kj} - S_{jk} S_{ki}) \right) \right], \quad (9)$$

where

$$\Omega_{ij} = \xi_{x_j}^k \frac{\partial U_i}{\partial \xi^k} - \xi_{x_i}^k \frac{\partial U_j}{\partial \xi^k},$$

u_t and ℓ_t are turbulence velocity and length scales, respectively, and α_4 and α_5 are model constants. The second constitutive relation was proposed by Craft et al. [15] (CLS) and involves non-linear terms up to cubic order:

$$\begin{aligned}
 \overline{u_i u_j} = & \frac{2}{3} k \delta_{ij} - \nu_t \left\{ S_{ij} - \frac{\ell_t}{u_t} \left[c_1 (S_{ik} S_{kj} - \frac{1}{3} S_{pq} S_{pq} \delta_{ij}) + c_2 (\Omega_{ik} S_{kj} + \Omega_{jk} S_{ki}) \right. \right. \\
 & \left. \left. + c_3 (\Omega_{ik} \Omega_{kj} - \frac{1}{3} \Omega_{pq} \Omega_{pq} \delta_{ij}) \right] \right. \\
 & \left. - \left(\frac{\ell_t}{u_t} \right)^2 \left[c_4 C_\mu (S_{ki} \Omega_{ij} + S_{kj} \Omega_{li} - \frac{2}{3} S_{km} \Omega_{lm} \delta_{ij}) S_{kl} + c_6 C_\mu S_{ij} S_{kl} S_{kl} \right. \right. \\
 & \left. \left. + c_7 C_\mu S_{ij} \Omega_{kl} \Omega_{kl} \right] \right\} \quad (10)
 \end{aligned}$$

where c_1 to c_7 and C_μ are model coefficients.

The turbulence velocity and length scales in the above constitutive equations, which are also used to calculate the eddy viscosity, are obtained by solving transport equations for the turbulence kinetic energy ($u_t = \sqrt{k}$) and an appropriate length-scale determining variable. We summarize here two of the most popular approaches for determining these scales, the standard k - ε model and the k - ω model—where ε is the rate of dissipation of k and ω is the specific energy dissipation (dissipation per unit kinetic energy).

The k - ε model

The vectors in eqn. (6) for the k - ε model as defined as follows:

$$\begin{aligned}
 Q_t = & [k \quad \varepsilon]^T, \quad F_t^j = \frac{V^j}{J} Q_t, \quad F_{\nu}^j = \frac{g^{mj}}{J \text{Re}} \frac{\partial}{\partial \xi^m} (Q_t), \\
 F_{tr}^j = & \left[\frac{\nu_t}{\sigma_k} \frac{g^{ij}}{J} \frac{\partial k}{\partial \xi^i}, \quad \frac{\nu_t}{\sigma_\varepsilon} \frac{g^{ij}}{J} \frac{\partial \varepsilon}{\partial \xi^i} \right]^T, \quad H_t = \frac{1}{J} \left[P - \varepsilon, \quad C_{\varepsilon 1} \frac{\varepsilon}{k} P - C_{\varepsilon 1} \frac{\varepsilon^2}{k} \right]^T, \quad (11)
 \end{aligned}$$

The constants used in this "standard" k - ε model are $C_\mu=0.09$, $C_{\varepsilon 1}=1.44$, $C_{\varepsilon 2}=1.92$, $\sigma_k=1.0$, and $\sigma_\varepsilon=1.3$, and the eddy-viscosity and the turbulence length scale are computed as follows:

$$\nu_t = C_\mu \frac{k^2}{\varepsilon} \quad \text{and} \quad \ell_t = \frac{k^{3/2}}{\varepsilon}. \quad (12)$$

The "standard" k - ε model is typically employed in conjunction with wall functions—in the subsequently presented applications we employ the two-point wall-functions approach of Patel et al. [27]. Several variants of the k - ε model that are applicable all the way to the wall, so-called low Reynolds number models, have also been proposed in the literature (see Patel et al. [28] for a review). Here we employ a version of the k - ε model that is applicable all the way to the wall but employs a two-layer treatment to model the near-wall region [16]. According to this approach, the flow domain is divided into two regions—the inner layer and the outer layer. The inner layer includes the sublayer, the buffer layer and part of the fully turbulent or logarithmic layer. A simple one-equation model is employed to account for the wall-proximity effects, whereas the standard, two-equation k - ε model is used in the outer layer. The details of this approach can be found in Chen and Patel [16].

The k - ω model

The vectors in eqn. (6) and the eddy-viscosity and turbulence length scale for the k - ω model of Wilcox [17] are defined as follows:

$$\begin{aligned} Q_t &= [k \quad \omega]^T, \quad F_t^j = \frac{V^j}{J} Q_t, \quad F_{\nu}^j = \frac{g^{mj}}{J \text{Re}} \frac{\partial}{\partial \xi^m} (Q_t), \\ F_{\nu}^j &= \left[\sigma^* v_t \frac{g^{ij}}{J} \frac{\partial k}{\partial \xi^i}, \quad \sigma v_t \frac{g^{ij}}{J} \frac{\partial \omega}{\partial \xi^i} \right]^T, \\ H_t &= \frac{1}{J} \left[P - \beta^* k \omega, \quad \alpha \frac{\omega}{k} P - \beta \omega^2 \right]^T, \end{aligned} \quad (13)$$

$$v_t = \alpha^* \frac{k}{\omega} \quad \text{and} \quad \ell_t = \frac{\sqrt{k}}{\omega}, \quad (14)$$

where the coefficients α , α^* , and β^* are either constants, for the high Reynolds number version of the model [17], or functions of the turbulence Reynolds number ($Re_t = k/\omega\nu$), for its low Reynolds numbers counterpart [29], and β , σ , and σ^* are constants [17, 29].

The $k-\omega$ model described above is employed in conjunction with the linear constitutive law given by eqn. (8). Non-linear versions of the $k-\omega$ model employing the SG, eqn. (9), and CLS, eqn. (10), constitutive equations have been proposed by Abid et al. [30] and Sofialidis & Prinos [31], respectively. In subsequent sections, we present results from all three versions: the standard linear model ($k-\omega$), and the two non-linear variants ($k-\omega(\text{GS})$ and $k-\omega(\text{CLS})$).

At hydraulically smooth solid boundaries, ω is specified by adopting the condition proposed by Menter [32]:

$$\omega = 800 \frac{V}{n^2},$$

where n is the normal distance of the first grid node off the wall. This condition works well as long as the first grid surface off the wall is located at $n^+ \leq 3$. For hydraulically rough surfaces, ω can be described using the boundary condition proposed by Wilcox [17] (see Neary et al. [33] for applications of the $k-\omega$ model to three-dimensional, separated flows over rough surfaces).

3 Numerical Solution of the RANS Equations

There are two general approaches for solving the incompressible RANS eqns: pressure-based, or pressure-Poisson methods, and the artificial compressibility approach. In our research we have successfully employed both approaches.

Sotiropoulos and Patel [4 – 7] extended the pressure-based formulation of Sotiropoulos and Abdallah [34] to solve the RANS equations in conjunction with full Reynolds-stress transport closures. This method discretizes the non-conservative form of the governing equations on a non-staggered mesh using second-order accurate finite-difference formulas. The discrete continuity equation is satisfied by solving a discrete pressure-Poisson equation tailored to eliminate the odd-even decoupling of the pressure nodes and minimize errors in the discrete continuity equation [34]. The mean momentum and turbulence closure equations are integrated in time using a four-stage, Runge–Kutta

time-stepping algorithm, enhanced with implicit residual smoothing and local time-stepping, while the ADI method is used to solve the pressure equation. The method of Sotiropoulos and Patel was applied successfully to a number of complex, three-dimensional, turbulent flows, including strongly curved ducts of regular and arbitrary cross-section [4, 35], a straight circular-to-rectangular transition duct [5, 6], and complex ship hulls [7].

An artificial compressibility approach was developed by Lin and Sotiropoulos [18, 19]. This method discretizes the strong-conservation form of the governing equations, on non-staggered grids, using central, and upwind (flux-difference splitting based) finite-volume schemes. The discrete equations are integrated in time using a novel strongly coupled multigrid procedure, which applies multigrid acceleration simultaneously to the mean flow and turbulence transport equations. The method has been applied in conjunction with both linear [18] and non-linear [8] near-wall, two-equation models with a great deal of the success. It is more robust and efficient than the non-conservative, finite-difference method of Sotiropoulos and Patel and appears very promising for handling highly stretched and skewed curvilinear meshes. A brief description of the main features of this approach is given in the following sections.

3.1 Spatial Discretization and Artificial Dissipation

The mean flow and turbulence closure equations, eqns. (1) and (6), respectively, can be coupled together and formulated in vector form as follows:

$$\frac{1}{J} \frac{\partial Q}{\partial t} + \frac{\partial}{\partial \xi^j} (F^j - F_V^j - F_T^j) - H = 0 \quad (15)$$

where

$$Q = \begin{bmatrix} Q_f \\ Q_t \end{bmatrix}, \quad F^j = \begin{bmatrix} F_f^j \\ F_t^j \end{bmatrix}, \quad F_V^j = \begin{bmatrix} F_{f_v}^j \\ F_{t_v}^j \end{bmatrix}, \quad F_T^j = \begin{bmatrix} F_{f_{rs}}^j \\ F_{t_r}^j \end{bmatrix}, \quad H = \begin{bmatrix} H_f \\ H_t \end{bmatrix},$$

and H_f is the zero vector of dimension four.

A semi-discrete approximation of eqn. (15) can be written as follows:

$$\frac{1}{J} \frac{dQ_{i,j,k}}{dt} + \delta_{\xi^1} (F^1 - F_V^1 - F_T^1)_{i,j,k} + \dots + H_{i,j,k} = 0, \quad (16)$$

where for clarity only derivatives in the ξ^l direction are shown and the discrete operator δ is defined as follows:

$$\delta_{\xi^1} ()_{i,j,k} = \frac{()_{i+1/2,j,k} - ()_{i-1/2,j,k}}{\Delta \xi^1}. \quad (17)$$

The viscous and turbulence (which include the Reynolds-stress terms in the momentum equations and the turbulence diffusion terms in the closure equations) fluxes at the cell faces as well as the velocity derivatives at the cell centers, necessary for calculating the source terms in the turbulence closure equations, are discretized using second-order accurate central-differencing. The convective fluxes, on the other hand, can be approximated in the following general manner:

$$\tilde{F}_{i\pm 1/2,j,k}^1 = \frac{1}{2} (F_{i,j,k}^1 + F_{i\pm 1,j,k}^1) + DISS_{i\pm 1/2,j,k}^1, \quad (18)$$

where *DISS* is an artificial dissipation flux necessary for eliminating odd-even (grid-scale) oscillations associated with the dispersive three-point central-differencing (obtained from eqn. (18) by setting *DISS*=0). Three different approaches for constructing such dissipative flux are considered in this study:

central-difference with scalar dissipation (CDS scheme),

$$DISS_{i+1/2,j,k}^1 = \varepsilon_{ad} \delta_{\xi^1} \left[\phi^1 \delta_{\xi^1} \delta_{\xi^1} \right] \left(\frac{Q}{J} \right)_{i+1/2,j,k}; \quad (19)$$

central-difference with matrix-valued dissipation (CDM scheme),

$$DISS_{i+1/2,j,k}^1 = \varepsilon_{ad} \delta_{\xi^1} \left[|A^1| \delta_{\xi^1} \delta_{\xi^1} \right] \left(\frac{Q}{J} \right)_{i+1/2,j,k}; \quad (20)$$

3rd-order flux-difference splitting (FDS3 scheme),

$$DISS_{i+1/2,j,k}^1 = \frac{1}{6} \left\{ \delta_{\xi^1} \left[A^{1-} \delta_{\xi^1} \left(\frac{Q}{J} \right) \right]_{i+1,j,k} + \delta_{\xi^1} \left[A^{1+} \delta_{\xi^1} \left(\frac{Q}{J} \right) \right]_{i,j,k} \right\}, \quad (21)$$

where ε_{ad} is a positive constant which controls the amount of dissipation, and ϕ^1 is a scaling factor along the ξ^1 -coordinate which is proportional to the spectral radius of the Jacobian matrix $A^1 = \partial F^1 / \partial Q$. For more details and the definitions and precise form of ϕ^j and the $|A^1|$ and $(A^1)^\pm$ matrices for the incompressible Navier–Stokes equations the reader is referred to Lin and Sotiropoulos [19].

All three schemes described above are implemented for discretizing the convective terms in the mean flow equations. The turbulence closure equations are discretized using upwind differencing, even when central-differencing is employed for the mean flow equations. For computations involving fully developed approach flow conditions, where the turbulence quantities vary smoothly away from the wall, third-order upwinding has been used successfully [18]. For developing boundary layers, on the other hand, the steep gradients of the turbulence quantities at the outer part of the boundary layer were found to give rise to non-physical oscillations when higher-order upwind differencing was employed to discretize the convective terms in the model equations. In such cases, we have found it necessary to employ first-order upwind differencing [8]. The very successful computations reported by Sotiropoulos and Ventikos [8] using this practice suggest that the so resulting reduction in spatial accuracy does not have a significant impact on the overall accuracy of the computed flowfield. As discussed in Sotiropoulos and Patel [7], the turbulence closure equations are driven primarily by their source terms, which, in all our computations, are discretized with second-order accurate schemes.

3.2 Coupled Runge–Kutta Algorithm

A pointwise-implicit, four-stage Runge–Kutta algorithm, enhanced with implicit residual smoothing and local time-stepping, is employed to advance the coupled mean flow and turbulence closure equations (eqn. (16)) in time. The iterative algorithm (see Lin and Sotiropoulos [18] for details) can be formulated as follows (for $m = 1$ to 4):

$$\begin{aligned} \mathfrak{S}[\Delta Q^{(m)}] &= -\gamma_p \Delta t J (I + \gamma_m \Delta t J B^{m-1})^{-1} RHS^{(m-1)}, \\ Q^{(m)} &= Q^{(n)} + \Delta Q^{(m)}, \end{aligned} \quad (22)$$

where $Q^{(o)}=Q^{(n)}$ and $Q^{(4)}=Q^{(n+1)}$, n denotes the current time level, γ_m are the Runge–Kutta coefficients, Δt is the time increment (calculated using local time-stepping [18]), B is the Jacobian matrix of the vector containing only the positive contributions to the source term H ($B = \partial H^+ / \partial Q$), \mathfrak{S} is the standard implicit residual smoothing operator, and RHS is the residual vector. The implicit treatment of the positive part of the source term H , which makes the basic Runge–Kutta algorithm pointwise implicit, was found to be essential for obtaining stable solutions, particularly when using ω -based models. The resulting matrix that needs to be inverted to compute the right hand side of eqn. (22) is of simple structure and its inversion is carried out analytically.

3.3 Multigrid Acceleration Strategy

The convergence rate of the above time-stepping algorithm can be greatly enhanced, particularly on stretched, large-aspect-ratio grids, by employing the multigrid acceleration technique. In our work, we have adopted the non-linear full approximation storage scheme (FAS) [36] in conjunction with the multigrid strategy developed by Jameson [37], for the solution of the Euler equations, and extended them to solve the coupled system of mean flow and turbulence closure equations.

The previously described Runge–Kutta algorithm (eqns. (22)), is employed as the basic smoother. A series of successively coarser grids is constructed by doubling the grid spacing either along all three spatial directions (full-coarsening strategy) or along only some spatial coordinates (semi-coarsening). Starting with an estimate of the solution on the finest mesh, the flow variables are transferred (or restricted) to the coarser grid using injection, that is, a transfer operator $T_{2h,h}^s$ which picks flow variables at alternate points to define coarse grid flow data as well as the coarse grid coordinates:

$$Q_{2h}^{(n)} = T_{2h,h}^s Q_h, \quad (23)$$

where the subscripts h and $2h$ denote fine and coarse mesh values, respectively. To ensure that the coarse grid solution is driven by fine mesh residuals—so that the reduced coarse-mesh accuracy does not contaminate the accuracy of the fine-mesh solution—the equations solved on the coarse mesh are modified by including a forcing term \wp_{2h} defined as follows [37]:

$$\wp_{2h} = T_{2h,h}^r R_h(Q_h) - R_{2h}(Q_{2h}), \quad (24)$$

where T^r is the residual restriction operator which computes a coarse grid residual by averaging the fine-grid residuals over the 27 fine-mesh nodes surrounding a coarse-mesh node [37]. The solution on the coarse mesh is then advanced in time using the Runge–Kutta algorithm in conjunction with implicit residual smoothing (eqn. (22)) as follows (for $m=1,2,3,4$):

$$Q_{2h}^{(m)} = Q_{2h}^{(n)} - \gamma_p \Delta t J \mathfrak{S}^{-1} \left(I + \gamma_m \Delta t J B^{m-1} \right)^{-1} \left(RHS_{2h}^{(m-1)} + \wp_{2h} \right). \quad (25)$$

Once the coarsest grid is reached, the accumulated corrections are transferred (or prolonged) back to the finest grid using a series of simple trilinear interpolations on successively finer grids. On highly stretched meshes, this interpolation procedure (which is carried out in the transformed, equally spaced, computational domain) may introduce

high-frequency errors back to the fine-mesh and result in degradation of the convergence rate. To eliminate such errors, the corrections on a given coarse mesh are processed through a constant-coefficient, implicit residual smoothing operator before using them to update the solution on the finer mesh.

A three-level V-cycle with subiterations is used in the present study for each time step on the finest mesh. One iteration is performed on the h grid, two on the $2h$ grid, and three on the $4h$ grid.

The turbulence closure equations are driven primarily by their source terms. It is, therefore, essential that these terms are represented accurately on the coarse meshes in order to maintain a rapid convergence rate. Obviously, the production term P cannot be resolved correctly on a coarse mesh since it involves velocity gradients which become very large in the vicinity of the wall. For that reason, the velocity gradient terms required for constructing P are computed only on the finest mesh and restricted by injection to all coarse meshes where they are kept frozen throughout the multigrid cycle. The eddy-viscosity, however, is updated continuously at all grids at the end of every Runge–Kutta stage.

The algorithm outlined above is a strongly coupled solution procedure since residual smoothing and multigrid acceleration are applied simultaneously to both the mean flow and turbulence closure equations. The other alternative for simulating turbulent flows is the so-called loosely coupled approach in which multigrid acceleration is applied to the mean flow equations, while the turbulence closure equations are solved only on the finest mesh [18]. This approach was found to be particularly useful for obtaining a well conditioned initial guess for the strongly-coupled algorithm. The latter is sensitive to the initial guess and its implementation can lead to numerical instability during the early stages of the calculation. The loosely coupled algorithm, on the other hand, is more robust during the initial stages and is always employed to start the computation. Typically 50 loosely coupled multigrid cycles are carried out before the strongly coupled procedure is activated.

3.4 Numerical accuracy and efficiency assessment studies

In this section we evaluate the performance of the algorithm described above by discussing results from computations of complex, three-dimensional flows. We emphasize both the spatial accuracy of the various discretization schemes presented in Section 3.1 and the overall efficiency of the strongly coupled multigrid procedure. Both issues are critical for the numerical computation of complex flows with advanced turbulence models. Excessive levels of artificial dissipation in a numerical algorithm can mask the effects of the turbulence model, thus making it very difficult to assess its true performance. On the other hand, iterative procedures that cannot handle stiff computational grids efficiently, such as those needed for resolving the near-wall layer, could require prohibitively large computational times for obtaining converged solutions.

3.4.1 Spatial accuracy

The performance of various artificial dissipation models described in Section 3.1 was evaluated in laminar and turbulent flow computations by Lin and Sotiropoulos [18, 19].

The laminar flow [19] tests were conducted for flow through a 90° strongly curved, square bend, using four successively finer grids: grid 1 (61×41×21), grid 2 (61×57×29), grid 3 (121×57×29), and grid 4 (151×97×49)—due to symmetry, only half of the cross-section was simulated. To eliminate uncertainties associated with accuracy loss on stretched meshes, the grid nodes, for all four grids, were distributed uniformly in the cross-plane. The effects of artificial dissipation on the accuracy of the computed solution is best underscored by Figure 1, which shows the radial velocity profile at the plane of symmetry at the end of curvature ($\theta=90^\circ$). The CDS and CDM (both implemented with $\epsilon_{ad}=0.004$) predictions, are on all grids within 20% of the finest mesh values. For the FDS3 scheme, on the other hand, differences as high as 75% are observed between the coarse and fine mesh solutions. Notice, in particular, that grids 2 and 3 produce practically identical results. Yet the strength of the secondary motion changes by approximately 45% when the finest mesh is employed. The most surprising trend from these comparisons is the extreme sensitivity of the FDS3 scheme to grid

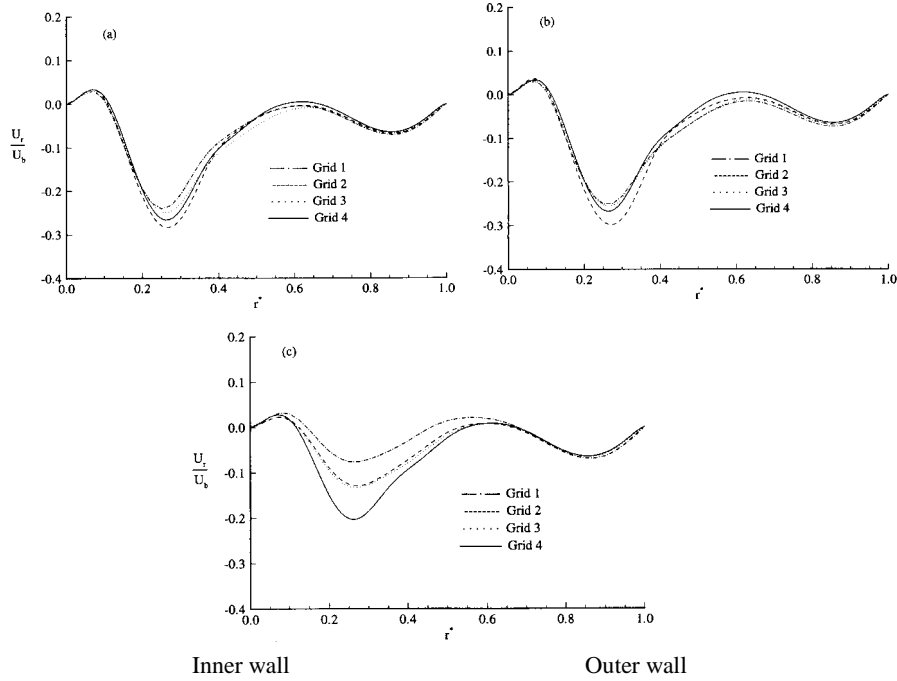


Figure 1: Effect of grid refinement on radial velocity profiles plotted along radial lines on the plane of symmetry at $\theta=90^\circ$. Laminar flow through a square, 90° bend. (a) CDS; (b) CDM; (c) FDS3.

resolution. To explore the reasons for this trend, Figure 2 shows the variation of the discrete divergence of the velocity field—calculated for all cases using central differencing—with respect to the reciprocal of an average grid density ($N^{-1/3}$). In other words, Figure 2 shows the amount of artificial dissipation that each of the three schemes introduces into the discrete continuity equation. The rate of reduction of the error with increasing grid density is consistent with the formal order of accuracy of each scheme. However, the artificial dissipation term introduced by the FDS3 scheme is consistently one order of magnitude larger than those of the two central-differencing schemes. It is important to point out that the large errors produced by the FDS3 scheme are due to the uniform mesh

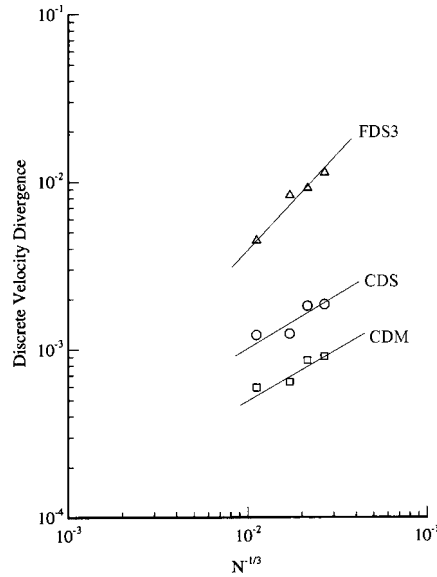


Figure 2: Effect of grid refinement on the average, over all grid nodes, absolute value of the discrete divergence of the velocity field. Laminar flow through a square, 90° bend.

used to discretize the duct cross-section. Refinement studies on grids that are stretched near the duct walls show that the FDS3 scheme gives very similar results to those obtained using the central differencing schemes (see also Figure 3 below). This trend suggests that the FDS3 scheme is rather dissipative in regions of high-velocity gradients but, as one would expect, the so-induced errors can be eliminated by local clustering of the grid lines.

These grid refinement studies were carried out on uniform cross-sectional grids for which the cell aspect ratios are close to unity. To assess the effect of artificial dissipation on large-aspect-ratio meshes, typical in turbulent flow calculations, we show in Figure 3 the results of several computations of turbulent flow through a 180° pipe bend. For all simulations we have employed the isotropic $k-\omega$ model. A highly

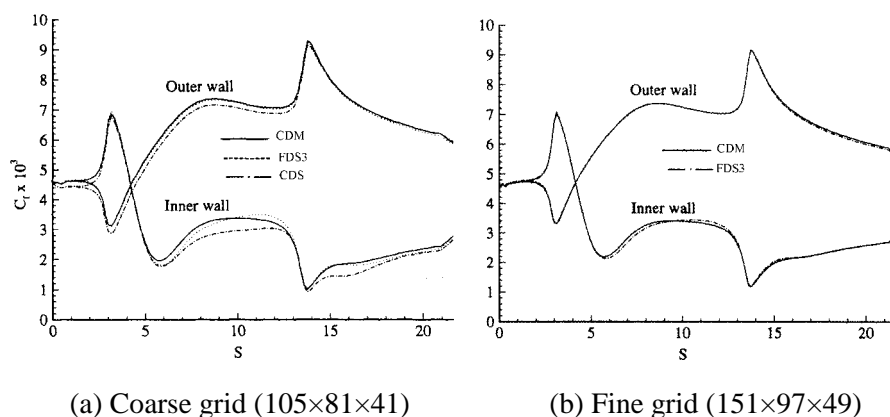


Figure 3: Effects of grid refinement and artificial dissipation model on the C_f distribution along the inner and outer walls of a 180° pipe bend at the plane of symmetry ($k-\omega$ model). (S is the arc length along the duct centerline)

stretched and skewed, curvilinear mesh was employed to discretize the pipe cross-section [18]. Computations were carried out on two grids: a coarse grid, with $105 \times 81 \times 41$ nodes, and a fine grid with $151 \times 97 \times 49$ nodes. The assessment of the various artificial dissipation models is carried out in terms of the computed skin-friction distribution along the inner and outer walls of the bend at the plane of symmetry. As seen in Figure 3a, on the coarse grid all three schemes produce similar qualitative trends but important quantitative differences are observed especially along the inner wall of the bend and the downstream tangent. The CDM and FDS3 schemes produce very similar results but the CDS predictions appear to be consistently lower almost everywhere and do not capture the sharp increase of the skin-friction at the downstream tangent along the inner wall of the bend. This inaccurate prediction is probably due to the anisotropic scaling employed in the construction of the CDS fluxes (introduced in the ϕ^j factor in eqn. (19)), which could introduce excessive levels of dissipation in the direction normal to the wall. On the fine mesh (see Figure 3b) the CDM and FDS3 schemes yield solutions that are practically indistinguishable from each other, as should be expected for consistent discretization schemes.

The previous comparisons underscore, among others, the fact that grid refinement studies in complex, three-dimensional flows should be carried out with a great deal of care and always by considering the physics of the flow. As shown in Figure 3, for instance, all three discretization schemes yield similar results along the outer wall of the bend. Yet, in the vicinity of the inner wall, where the pressure-driven secondary flows give rise to very complex flow patterns, there are significant discrepancies between the three predictions. That is, when performing grid sensitivity studies it is essential to consider the effect of grid refinement in regions of the flow where the most complex phenomena occur. Examining the sensitivity of the solutions in relatively "simpler" regions of the flowfield could lead to misleading results.

3.4.2 Assessment of Multigrid Performance

To demonstrate the performance of the multigrid procedure described in Section 3.2, we discuss here some of the results reported by Lin and Sotiropoulos [18]. The test case is the same 180° pipe bend for which computed skin-friction profiles are shown in Figure 3. For both the coarse (350,000 node) and fine (720,000 node) meshes, three to four grid nodes have been placed within the laminar sublayer ($n^+ < 5$) with the first grid surface off the wall located at $n^+ = 1$. The isotropic, low Reynolds number $k-\omega$ model has been used for closure and the computations have been carried out for $Re = 60,000$, based on the bulk velocity and the pipe diameter.

Figure 4a compares the convergence histories for the single and multigrid methods. The single-grid algorithm is employed only in conjunction with the FDS3 scheme on the coarse mesh. The convergence of the multigrid method, on the other hand, is reported for both the CDM and FDS3 discretization schemes and the coarse and fine meshes. It should be pointed out that all multigrid convergence histories shown in this figure are obtained using the strongly coupled algorithm with coarsening applied only in the cross-plane (semi-coarsening). As seen, regardless of discretization scheme and mesh size, the multigrid algorithm converges at approximately the same rate. Converged, to plotting scale, solutions are obtained after the residuals have dropped by approximately four orders of magnitude [18]. This convergence level is

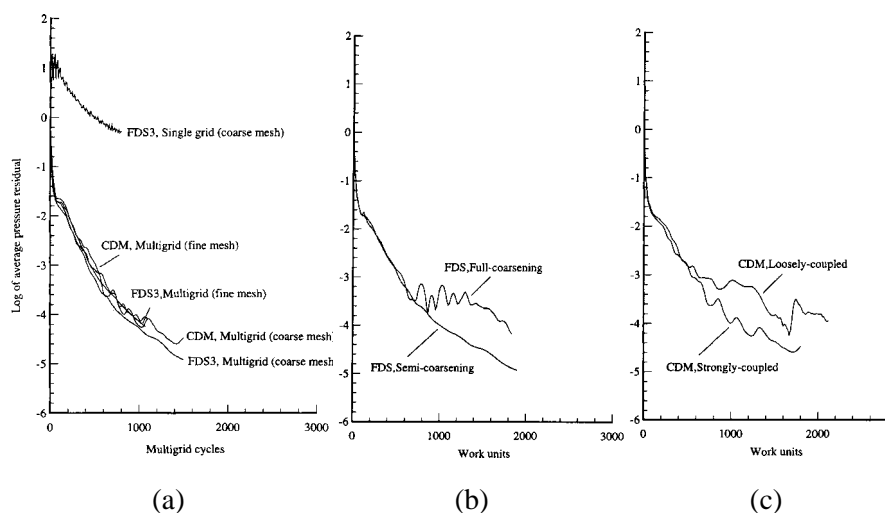


Figure 4: (a) Convergence histories for single and multi-grid algorithms; (b) effect of grid coarsening on multigrid performance; (c) loosely vs. strongly coupled multigrid for solving the turbulence closure equations ($k-\omega$ model). Mesh sizes are defined in Figure 3.

achieved within 800 and 900 multigrid cycles on the coarse and fine meshes, respectively. The single-grid algorithm, on the other hand, converges at a dramatically slower rate as the residual drops by only 1.2 orders of magnitude after 800 time steps. Due to the excessive computational resources that would be required to reach convergence, the calculations were stopped after 800 time steps. Comparison of the solution at this point with the converged multigrid solution indicates that the single-grid algorithm would require several thousands of iterations to reach steady state. This is also evident from the continuously declining slope of the single-grid convergence curve. Concerning the effect of artificial dissipation on multigrid performance, it is seen that both schemes converge at similar rates. In another study, Lin and Sotiropoulos [19] assessed the relative performance of the two schemes for laminar flow through a curved duct and showed that both CDM and

FDS3 schemes require approximately the same number of cycles to reduce the residual by four orders of magnitude. However, the CDM scheme slowed down beyond that point, never reaching machine zero which was achieved by the FDS3 scheme. Although the present calculations were not continued long enough, a similar trend is visible in Figure 4 as the CDM scheme appears to slow down, somewhat, beyond 1000 cycles.

The effect of grid-coarsening on the efficiency of the strongly coupled multigrid algorithm is shown in Figure 4b, which depicts the convergence histories for full- and semi-coarsening strategies using the FDS3 scheme (similar trends were observed with the CDM scheme as well). Both coarsening strategies converge at exactly the same rate during the first 800 work units. Beyond this point, however, the full-coarsening algorithm slows down significantly and requires approximately 1800 work units to reduce the residual by four orders of magnitude. Semi-coarsening, on the other hand, produces a monotonic convergence curve and requires approximately 80% less work to achieve convergence. It is evident, therefore, that semi-coarsening increases the performance of the multigrid algorithm significantly. Presumably this is because for geometries such as the pipe bend considered herein (where the grid spacing in the streamwise direction is more or less uniform) semi-coarsening produces coarse meshes with reduced cell aspect-ratios, thus enhancing the overall effectiveness of the multigrid technique.

The efficiency of the loosely and strongly coupled (SC) procedures for solving the turbulence closure equations can be gauged from Figure 4c. For the loosely coupled (LC) algorithm, three iterations are carried out on the finest grid for the turbulence closure equations at the end of every multigrid cycle for the mean flow equations. The work unit used in this figure has been appropriately scaled, according to CPU time, to account for this additional computational overhead. Obviously, adopting a strongly coupled treatment enhances the efficiency of the multigrid algorithm. With the strongly coupled treatment convergence is achieved within 1000 work units while the loosely coupled approach requires more than 1600 work units to reach a similar level of convergence.

4. Predictions of 3D shear flows with advanced turbulence closures

In this section we evaluate the relative performance of the various turbulence models presented in Section 2.2 by reviewing results from several simulations of complex, three-dimensional flows. The three test cases we discuss are among a handful of available experiments today that can be used for comprehensive model validation studies. In all subsequently presented computations, we have carefully minimized numerical uncertainties so that the true performance of the closure models can be readily assessed. For each case we consider, computations for all turbulence models have been carried out on identical numerical grids, using the same numerical method and boundary conditions, and employing the same convergence criteria.

The work reviewed here has been reported in a sequence of papers [5 – 8], which the interested reader should consult for more details.

4.1 Flow through a circular-to-rectangular transition duct

Davis and Gessner [38] carried out detailed, mean flow and Reynolds-stress measurements for the flow through a circular-to-rectangular (CR) transition duct (Figure 5) at Reynolds number $Re = 3.9 \times 10^5$, based on the bulk velocity and inlet diameter. The flow in the transition section is affected by the change in the cross-section shape and the associated wall curvatures, both longitudinal and transverse, by the initial diffusion and subsequent contraction due to change in area, and by the pressure gradients associated with these rapid changes. The measurements indicate that these factors, together, induce a pair of longitudinal vortices located near the vertical side wall. The contours of mean streamwise velocity, total pressure, and Reynolds stresses at the end of the transition region reveal significant distortion of the mean flow and turbulence structure in the vicinity of the vortex core.

Calculations were carried out using the numerical method of Sotiropoulos and Patel [5, 6] with three turbulence models: (i) the standard k - ϵ model with wall functions; (ii) the GL Reynolds-stress model; and (iii) the LSH Reynolds-stress model. Due to the symmetry

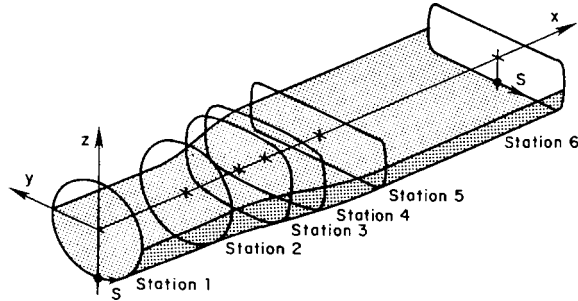


Figure 5: Coordinates and measurement locations for the transition duct of Davis and Gessner [38].

of the duct and the symmetric inlet-flow conditions, only one quadrant of the duct was simulated. The duct cross-section was discretized using a polar mesh layout. The grid lines were concentrated near the duct wall using a hyperbolic tangent stretching function. For the calculations with the two high Reynolds number models ($k-\varepsilon$ and GL), the first coordinate surface off the solid wall was located at approximately $n^+=70$, with ten points within $70 < n^+ < 120$. For the LSH computation, the first grid surface was placed at $n^+=0.5$, with ten points within the laminar sublayer and the buffer layer. Inlet conditions were specified using the measurements of Davis and Gessner [38].

Figure 6a shows the measured and calculated contours of the streamwise component of mean velocity at station 5. The measurements exhibit a region of low-velocity located near the junction between the horizontal plane of symmetry and the vertical wall, induced by the longitudinal vortex pair that forms as a result of the secondary motion. These vortices, with the common flow between them directed away from the side wall, transport low velocity fluid from the wall boundary layers towards the center of the cross-section. The $k-\varepsilon$ prediction fails to predict the distorted shapes of the measured isovels in the vicinity of the vortex-pair—in fact the calculated velocity contours do not exhibit any distortion at all. The GL closure, on the other hand, produces only a mild distortion of the velocity contours, while the LSH closure

reproduces the measurements of Davis and Gessner with remarkable accuracy.

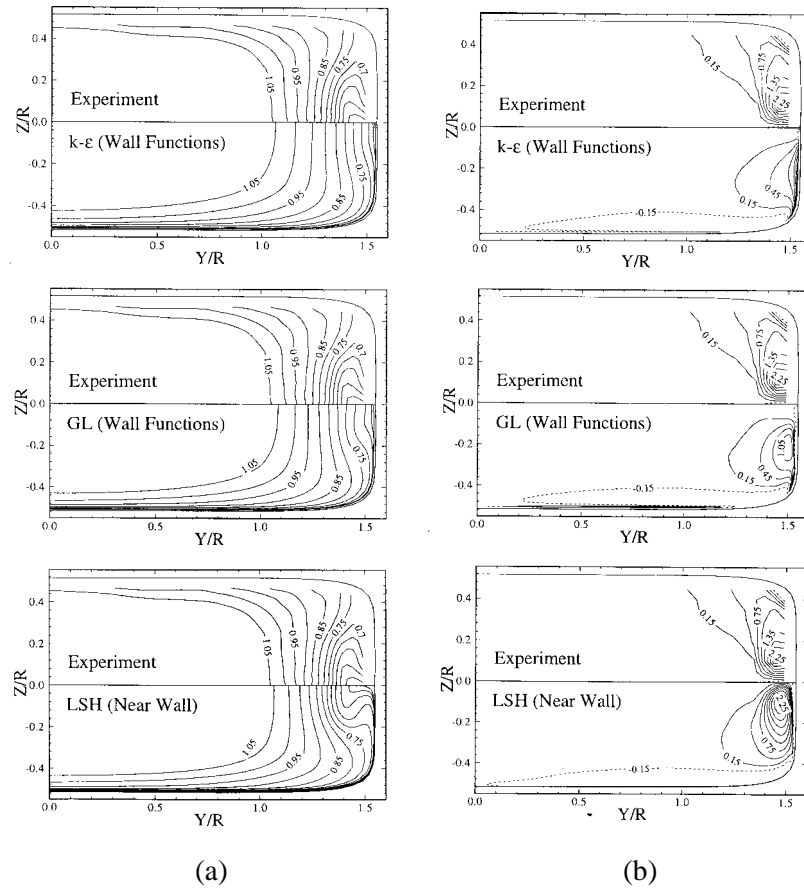


Figure 6: Measured and computed contours of (a) mean streamwise velocity and (b) mean streamwise vorticity at station 5.

The differences in the prediction of the streamwise velocity distribution should correlate with the ability of each closure to resolve the origin and growth of the secondary motion, which is best visualized through contours of the mean longitudinal vorticity ($\Omega_x R/U_b$). The experimental and computed contours at station 5 are shown in Figure 6b.

As anticipated from the predictions of the streamwise velocity, the secondary motion calculated by the k - ε closure does not lead to a distinct longitudinal vortex, while the GL closure predicts a well defined, although much weaker than measured, vortex. More specifically, the GL closure predicts a core vorticity value of about 1.1, which is about 50% smaller than that measured by Davis and Gessner. Furthermore, the location of the calculated vortex does not correspond to that indicated by the measurements—the calculated vortex being closer to the vertical wall and further away from the horizontal symmetry plane. Despite the failure of both closures (k - ε and GL) to reproduce the measured vorticity field, the fact that the GL closure produces a distinct longitudinal vortex indicates that the Reynolds-stress terms in the vorticity transport equation have become significant at the end of the transition region. Sotiropoulos and Patel [6] provided additional evidence to support such a conclusion. They employed the LSH solution, which is in excellent agreement with the measurements, to evaluate the various terms in the Reynolds-averaged longitudinal vorticity transport equation. They concluded that vortex stretching, vortex skewing, and generation and destruction of vorticity by Reynolds stresses are all dominant in one region or the other. Another important conclusion that follows from the above comparisons is that the wall-functions approach, whether it is used in isotropic or non-isotropic closures, is inadequate to resolve complex three-dimensional flows. Therefore, our findings suggest that accurate descriptions of most three-dimensional turbulent flows, regardless of the origin of three-dimensionality, would require the use of turbulence models that resolve the near-wall flow and account for the anisotropy of the Reynolds stresses.

To gauge the ability of the two Reynolds stress models to predict the distribution of individual Reynolds stresses, we show in Figure 7 profiles in wall coordinates of the three normal stresses and the primary shear stress along the horizontal and vertical planes of symmetry at station 5. With the only exception the overprediction of the normal stress by the GL closure, the two models yield similar results along the vertical plane of symmetry where the flow exhibits boundary layer characteristics. An entirely different picture emerges, however, along the horizontal plane of symmetry where the flow is distorted by the longitudinal vortices. The LSH closure, for instance, captures, both

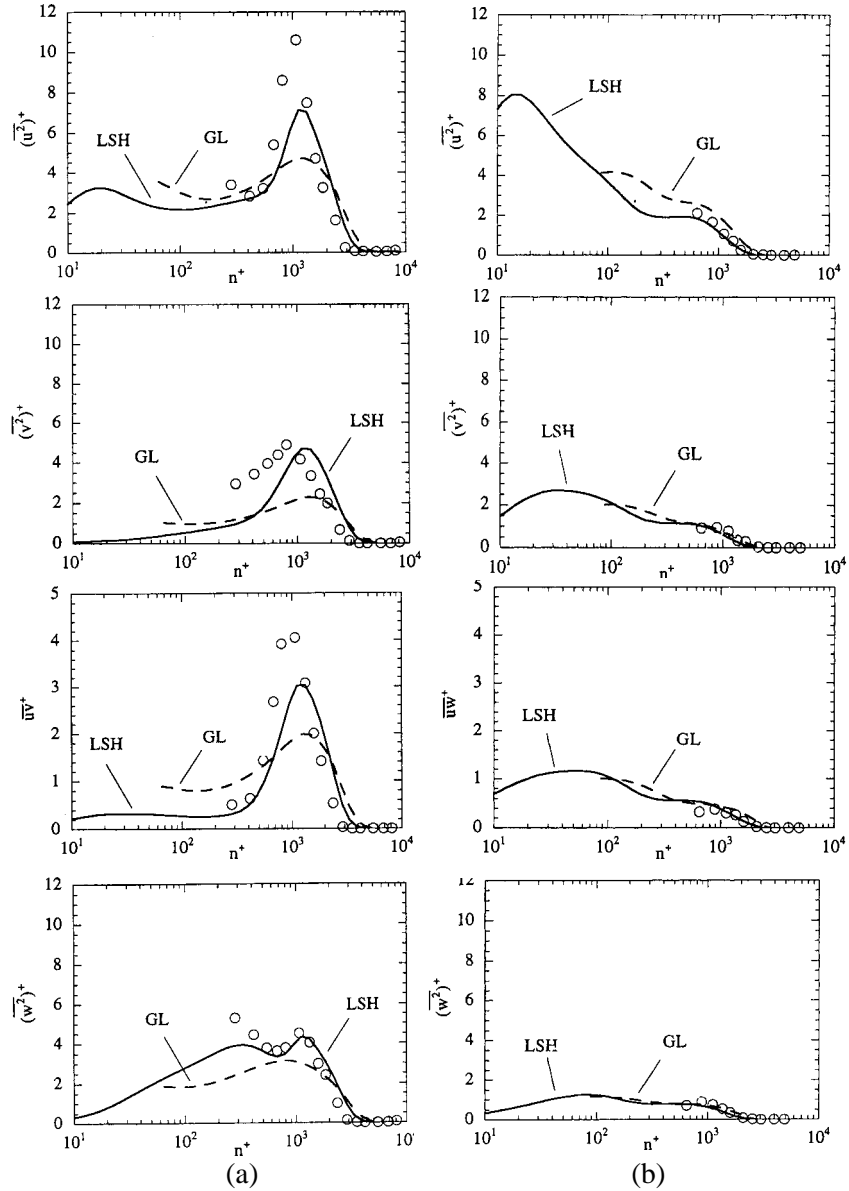


Figure 7: Measured (circles) and computed Reynolds-stress profiles in wall coordinates at station 5: (a) $z = 0$; (b) $y=0$.

qualitatively and quantitatively, almost all experimental trends. The GL closure, on the other hand, underpredicts the levels of all Reynolds-stresses in the vicinity of $n^+=1000$, which corresponds to the pocket of increased turbulence intensity observed in Figure 8 below, and does not capture the two peaks observed in the measured distribution of $\overline{w^2}^+$. Notice in particular the failure of the GL closure to predict correctly both the levels and the gradients of the Reynolds-stresses near $n^+=70$, where the wall-functions boundary conditions are applied. This failure further demonstrates the inadequacy of the wall-functions approach, and the local equilibrium assumptions associated with it, for simulating complex, non-equilibrium, shear flows.

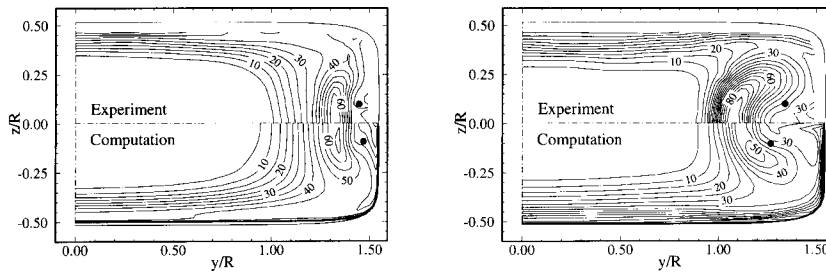


Figure 8: Measured and computed (LSH) contours of turbulence kinetic energy ($k / U_b^2 \times 10^4$) at stations 5 (left) and 6 (right).

An important weakness of the LSH closure is demonstrated in the comparisons of the turbulence kinetic energy shown in Figure 8. At station 5, the model reproduces the measured pocket of increased turbulence intensity, induced by the interaction of the vortex pair with the sidewall boundary layer, with remarkable accuracy. This trend is consistent with the predictions of the mean flow and individual Reynolds stresses discussed above. Between stations 5 and 6, however, the calculations predict an overall decay of turbulence kinetic energy, with the peak k value decreasing by approximately 15%. The measurements, on the other hand, reveal that the pocket of high turbulence kinetic energy is intensified, and the peak value of k increases by almost 38%. In light of the excellent agreement between the LSH predictions and the

measurements at station 5, this discrepancy is very surprising and unveils an important weakness of the model, namely its inability to predict correctly the relaxation of a rapidly strained turbulent flow towards equilibrium.

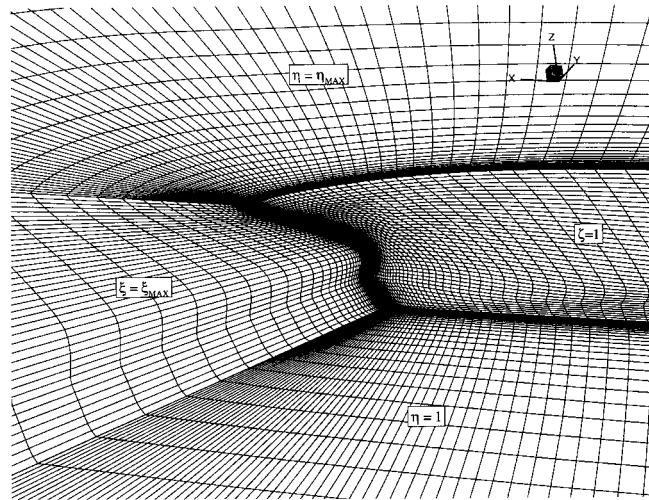


Figure 9: Typical view of the grid on hull's surface and surrounding boundaries (hull shown is the original HSVA tanker).

4.2 Prediction of flow in the stern and wake region of a tanker hull

The development of numerical methods capable of quantitatively accurate predictions of ship stern and wake flows has been the subject of intense research for several years. The rapid geometrical changes of typical hull shapes near the stern region give rise to very complex, three-dimensional flows that are dominated by strong longitudinal vortices. The sense of rotation of these vortices is such that they transport low momentum fluid from the thick boundary layer near the free-surface downward, creating a pocket of low streamwise momentum upstream of the marine propeller. In other words, the stern vortices determine, to a

large extent, the inflow to the propeller. Since propeller designers require quantitatively accurate descriptions of the approach flow, prediction of the strength of the stern vortices has become the litmus test for the ship hydrodynamics CFD community and has been a major focus of two international workshops during the past decade [39, 40]. The first successful predictions of the flow at the propeller plane of complex hull geometries were reported by Sotiropoulos and Patel [7].

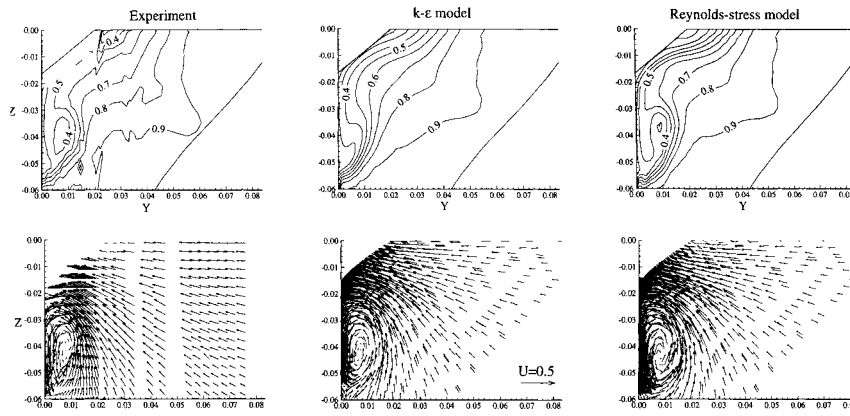


Figure 10: Axial velocity contours and cross-flow vectors at the propeller plane of the modified HSVA tanker (Mystery hull).

Simulations were carried out for the two tanker hull geometries that were used as test cases in the 1991 and 1994 workshops: (i) the HSVA tanker; and (ii) a modified HSVA tanker, known in the literature as the "mystery" hull. Both of these geometries are doubly symmetric bodies. Mean velocity and turbulence statistics measurements were carried out by Denker et al. [41] in a wind-tunnel—that is, free-surface effects were not considered, as the main emphasis was on the flow structure near the propeller. The computational domain and a typical view of the O-O type computational grid on the hull surface are shown in Figure 9. To demonstrate the importance of turbulence modeling for quantitatively accurate predictions of this flow, we performed calculations using the isotropic, two-layer $k-\epsilon$ model of Chen and Patel [16] and the LSH Reynolds transport model.

The measured and computed streamwise mean velocity contours and cross-flow velocity vectors at the propeller plane of the Mystery hull are shown in Figure 10. The two-layer $k-\epsilon$ model predicts fairly well the gross features of the flowfield but fails to reproduce the very pronounced low-velocity region in the central part of the wake. The LSH model, however, resolves correctly the distinct hook-shaped contours in this region and predicts, in agreement with the measurements, a stronger secondary motion.

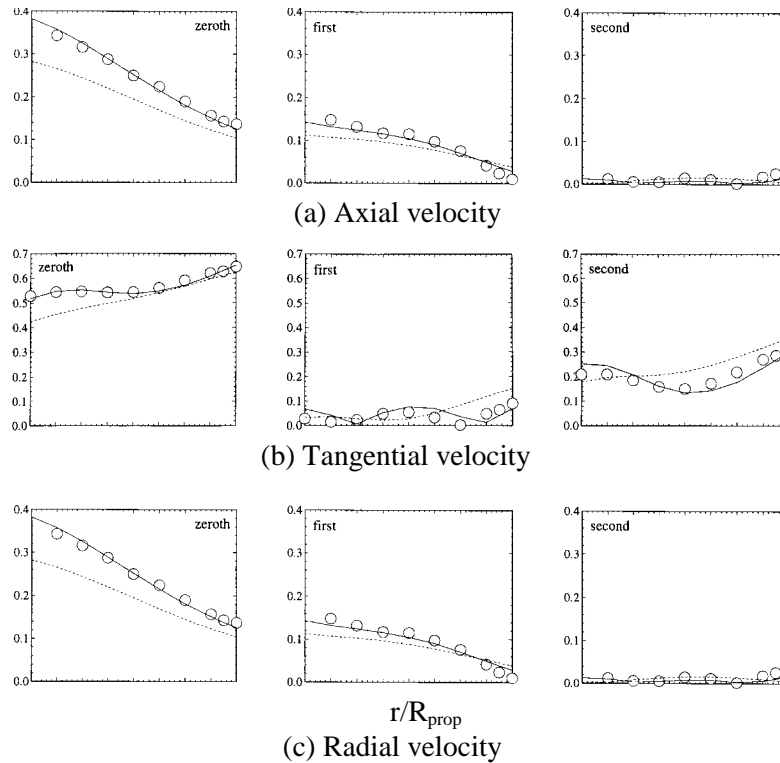


Figure 11: Amplitudes of first three harmonics of the velocity field at the propeller plane of the Mystery hull.

Solid line: LSH; dashed line: two-layer $k-\epsilon$; circles: data.

To further emphasize the importance of advanced turbulence modeling from the propeller designer standpoint, the measurements and computations were processed to obtain the amplitudes of the axial, radial, and tangential velocity harmonics at the propeller disk. Accurate predictions of the velocity harmonics is very important because this is precisely the kind of information that a propeller designer requires from a CFD computation. In Figure 11, we compare the measured and computed first three harmonics for each velocity component—for comparisons of additional harmonics see Sotiropoulos and Patel [7]. As seen the isotropic model fails to predict correctly even the zeroth harmonic for all three velocity components. The LSH model, on the other hand, reproduces the measurements with remarkable accuracy.

The above results further reinforce the conclusions reached in the transition duct case concerning the importance of modeling the effects of turbulence anisotropy in three-dimensional flow simulations. Even though in both cases we have examined thus far longitudinal vorticity originates via lateral skewing of the vorticity vector and is intensified by axial stretching (both "inviscid" mechanisms), the Reynolds stresses play a critical role in the evolution and subsequent decay of the so-produced vorticity field [6], and thus need to be carefully modeled.

4.3 Prediction of flow through a strongly curved rectangular bend

The examples reviewed in the previous sections underscore the tremendous promise of near-wall Reynolds-stress transport models for developing predictive methods for flows of engineering interest. In spite of their success, such models are not practical for simulating complex flows because they require the solution of seven additional transport equations. With the continuous improvement of efficient numerical methods and rapidly increasing supercomputer performance, this requirement may not be too restrictive for steady-state simulations. It could, however, prove to be prohibitively expensive in unsteady RANS/VLES simulations. Non-linear, two equation models offer a more realistic alternative in that regard as they can, at least in principle, account for the effects of turbulence anisotropy at a considerably lower overhead.

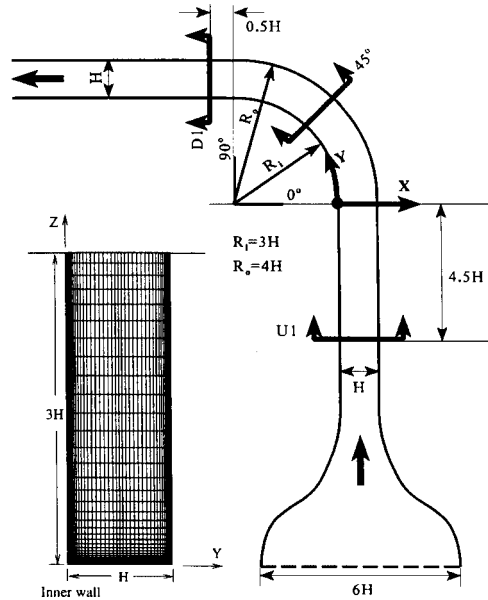


Figure 12: Coordinates, measurement locations, and cross-sectional mesh for the curved duct of Kim and Patel [42].

We evaluate here the performance of the two non-linear versions of the $k-\omega$ model described in Section 2.2.2, the $k-\omega(\text{SG})$ and the $k-\omega(\text{CLS})$, by applying them to calculate flow through a curved duct for which detailed experiments were reported by Kim and Patel [42]. The duct geometry along with a cross-sectional view of the computational grid are shown in Figure 12. The flow enters the inlet tangent of the curved duct through a short transition duct (a two-dimensional 6:1 contraction). The transverse pressure gradients on the top wall of the contraction induce a pair of vortices inside the top-wall boundary layer resulting in a complex three-dimensional flow at the inlet of the upstream straight tangent [42]. In order to ensure that the inlet conditions for the numerical calculations properly represent the experimental situation, the experimental data at station U1 are used to construct appropriate inlet distributions for the mean velocity components and the turbulent quantities. The details

concerning the specification of inlet conditions and other numerical issues are described in Sotiropoulos and Ventikos [8].

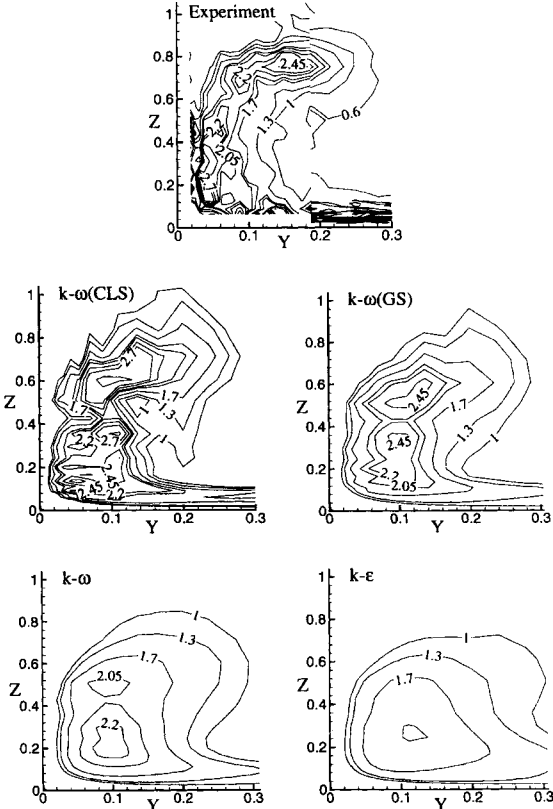


Figure 13: Measured and computed mean streamwise vorticity contours near the corner of the inner wall at station D1. Axis aspect ratios have been distorted for clarity.

The curvature-induced transverse pressure gradients set up a strong secondary motion that begins to grow near the top and bottom inner corners of the duct cross-section. This secondary motion is directed (along the horizontal endwalls) from the outer (concave) to the inner (convex) walls and distorts the inner wall boundary layer giving rise to a highly three-dimensional turbulent flow—via a mechanism similar to

that discussed above for the transition duct and the tanker hull. The complexity of the flow in that region is best demonstrated by examining the structure of the longitudinal mean vorticity contours near the lower left corner of the cross-section. Figure 13 shows measured (obtained by post-processing the data of Kim and Patel) and computed vorticity contours at station D1 (see Figure 12 for the station location and the coordinate definition). The computed results include predictions from the two non-linear variants of the $k-\omega$ model as well as from the isotropic $k-\omega$ and two-layer $k-\epsilon$ models. The measurements reveal a very complex vortex structure, characterized by the presence of several distinct local vorticity maxima and C-shaped contours—for clarity the axis aspect ratio in this figure has been distorted. The role of turbulence modeling in predicting these features is demonstrated in a very dramatic manner by the comparisons shown in Figure 13. The two-layer $k-\epsilon$ model fails to even capture the general qualitative structure of the measured contours. Although the accuracy of the computed results improves somewhat with the $k-\omega$ model, it is evident that neither isotropic closure can reproduce the complexities of the flow. Adopting a non-linear constitutive model, on the other hand, results in striking improvements. The $k-\omega$ (GS) model yields a much more intense (as compared to the isotropic model predictions) secondary motion but the vortex core is located further away from the wall and the overall structure of the contours is simpler than indicated by the measurements. A remarkable, considering the complexity of the flow, level of agreement with the experiment is obtained only when using the cubic $k-\omega$ (CLS) model. The computed contours are clearly C-shaped and the vortex core is characterized by several distinct local vorticity maxima and is located closer to the inner wall, as indicated by the measurements.

Detailed comparisons [8] between measured and calculated turbulence statistics in the vicinity of the vortex core, not shown herein due to space limitations, show that the $k-\omega$ (CLS) model captures the general qualitative and quantitative trends of the measured turbulence field reasonably well. An important systematic disagreement [8] was observed near the outer (concave) wall of the bend where none of the models employed herein succeeded in predicting the increased turbulence levels indicated by the measurements. Although the inability of standard two-equation models to predict the effects of concave

curvature is well known [9], this finding suggests similar inadequacies with non-linear models as well. This discrepancy notwithstanding, however, the results of this study are particularly encouraging. They demonstrate, for the first time, that a relatively simple, compared to a full Reynolds-stress transport model, two-equation closure is capable of resolving not only the mean flow but the general structure of the turbulence statistics in a very complex, highly three-dimensional shear flow.

5 Conclusions

The work reviewed herein underscores some of the progress made during the past decade in predicting three-dimensional, turbulent, shear flows of engineering interest. It is important to point out that the modeling state of affairs at the beginning of the 1990s was rather disappointing and was very succinctly summarized by Bradshaw [43] as “much a list of inadequacies as achievements.” Some ten years later, the continuously increasing comprehension of the structure of turbulence, derived from DNS and advancements in experimental techniques, the refinement of turbulence modeling strategies driven by this comprehension, and the increased sophistication of numerical methods and rapid advancements in computational power, have all contributed to the progress reported in this article.

The most important finding is that RANS methods in conjunction with advanced turbulence models, that resolve the near-wall flow and account for turbulence anisotropy, can indeed yield quantitatively accurate predictions, at least for the mean flow quantities, for complex, engineering flows. Particularly encouraging in this regard is the performance of non-linear, two-equation eddy-viscosity models, which provide a very cost-effective alternative to full, Reynolds-stress transport models. Such models are very promising candidates for building the next generation of unsteady RANS/VLES models, a subject which we expect to attract considerable research attention in the coming years.

In spite of the progress and the optimistic results reported herein, there are still significant areas where modeling refinements are needed. For instance, even the most advanced current methodologies cannot

predict the relaxation of rapidly strained turbulence toward equilibrium. Also the dramatic de-stabilizing effects of concave curvature cannot be accounted for by either Reynolds-stress transport or non-linear two-equation models without explicit curvature correction terms—most of which are only applicable to two-dimensional flows [9]. Most importantly, predictions of flows over rough surfaces at full scale Reynolds numbers, a subject not addressed in this review, still remains a major challenge for even the most advanced CFD techniques [44]. Addressing this issue will require the development of robust iterative algorithms that can handle efficiently the excessive numerical stiffness that is unavoidable in high Reynolds number simulations of complex flows with near-wall turbulence models. The strongly coupled multigrid methodology described herein is a promising framework for developing such methods. It should be enhanced considerably, however, with optimal grid-coarsening strategies, grid-embedding and domain decomposition techniques, and pre-conditioning techniques to remove numerical stiffness and enhance efficiency and robustness. These requirements for numerical algorithm enhancements will become even more critical if advanced turbulence models are to be extended to unsteady RANS/VLES simulations.

Finally, we should emphasize that an important factor to the progress reported herein was the access to high-quality experiments for complex, three-dimensional flows. In the past, testing and validation of advanced turbulence models was primarily restricted to relatively simple, two-dimensional shear flows. The first application, however, of such models to three-dimensional flows unveiled their tremendous potential, identified their weaknesses, and defined areas for future research. For further progress to be made, therefore, it is critical that experimental investigations as detailed as those reported by Davis and Gessner [38] and Kim and Patel [42] continue to enrich the literature.

Acknowledgements

I am grateful to V.C. Patel for his inspiring mentorship. His infectious enthusiasm for three-dimensional turbulent flows motivated most of the work reviewed herein. I also wish to acknowledge the financial support

of the National Science Foundation in the form of a CAREER award (CMS-9875691).

References

- [1] Speziale, C. G., Turbulence modeling for time-dependent RANS and VLES: A review, *AIAA Journal*, **36**, (2), pp. 173-184, 1998.
- [2] Wu, X., and Squires, K. D., Numerical investigation of the turbulent boundary layer over a bump, *Journal of Fluid Mechanics*, **362**, pp. 229-271, 1998.
- [3] Kaltenbach, H. J., Fatica, M., Mittal, R., Lund, T.S., and Moin, P., Study of flow in a planar asymmetric diffuser using large-eddy simulation, *Journal of Fluid Mechanics*, **390**, pp. 151-185, 1999.
- [4] Sotiropoulos, F., and Patel, V. C., Evaluation of some near-wall models for the Reynolds stress transport equations in a complex shear flow, *Near-Wall Turbulent Flows*, ed. R. M. C. So, C. G. Speziale, and B. E. Launder, Elsevier, New York, pp. 987-997, 1993.
- [5] Sotiropoulos, F., and Patel, V. C., Prediction of turbulent flow through a transition duct using a second-moment closure,"*AIAA Journal*, **32**, (11), pp. 2194-2204, 1994.
- [6] Sotiropoulos, F., and Patel, V. C., On the role of turbulence anisotropy and near-wall modeling in predicting complex, 3D, shear flows, *AIAA Journal*, **33**, (3), pp.504-514, 1995.
- [7] Sotiropoulos, F., and Patel, V. C., Application of Reynolds-stress transport models to stern and wake flows, *Journal of Ship Research*, **39**, (4), pp. 263-283, 1995.
- [8] Sotiropoulos, F., and Ventikos, Y., Flow through a curved duct using nonlinear two-equation turbulence models, *AIAA Journal*, **36**, (7), pp.1256-1262, 1998.
- [9] Patel, V. C., and Sotiropoulos, F., Longitudinal curvature Effects in turbulent boundary layers, *Progress in Aerospace Science*, **33**, pp. 1-70, 1997.
- [10] So, R. M. C., Lai, Y. G., Zhang, H. S., and Hwang, B. C., Second order near-wall turbulence closures: A review, *AIAA Journal*, **29**, (11), 1819, 1991.

- [11] Gibson, M. M., and Launder, B. E., Ground effects on pressure fluctuations in the atmospheric boundary layer, *Journal of Fluid Mechanics*, **86**, pp. 491-511, 1978.
- [12] Launder, B. E., and Shima, N., Second-moment closure for the near-wall sublayer: Development and application, *AIAA Journal*, **27**(10), pp. 1319-1325, 1989.
- [13] Shima, N., Prediction of turbulent boundary layers with a second-moment closure: Part I--Effects of periodic pressure gradient, wall transpiration, and free-stream turbulence, *Journal of Fluids Engineering*, **115**, (1), pp. 56-63, 1993.
- [14] Gatski, T. B., and Speziale, C. G., On explicit algebraic stress models for complex turbulent flows, *Journal of Fluid Mechanics*, **254**, pp. 59-78, 1993.
- [15] Craft, T. J., Launder, B. E., and Suga, K., Development and application of a cubic eddy-viscosity model of turbulence, *Int. J. Heat and Fluid Flow* **17**, (2), pp. 108-115, 1996.
- [16] Chen, H. C., and Patel, V. C., Near-wall turbulence models for complex flows including separation, *AIAA Journal*, **26**, (6), pp. 641-648, 1988.
- [17] Wilcox, D. C., Reassessment of the scale determining equation for advanced turbulence models, *AIAA Journal*, **26**, (11), pp. 1299-1310, 1988.
- [18] Lin, F., and Sotiropoulos, F., Strongly-coupled multigrid method for 3-D incompressible flows using near-wall turbulence closures, *ASME Journal of Fluids Engineering*, **119**, (2), pp. 314-324, 1997.
- [19] Lin, F., and Sotiropoulos, F., Assessment of artificial dissipation Models for three-dimensional, incompressible flow solutions, *ASME Journal of Fluids Engineering*, **119**, (2), pp. 331-340, 1997.
- [20] Demuren, A. O. & Rodi, W., Calculations of turbulence-driven secondary motion in non-circular ducts, *Journal of Fluid Mechanics*, **140**, 189-222, 1984.
- [21] Durbin, P. A., A Reynolds-stress model for near-wall turbulence, *Journal of Fluid Mechanics*, **249**, pp. 465-498, 1993.

- [22] Launder, B.E., and Li, S.P., On the elimination of wall topography parameters from second-moment closure, *Physics of Fluids*, **6**, pp. 999-1006, 1994.
- [23] Craft, T. J., and Launder, B. E., A Reynolds-stress closure designed for complex geometries, *Int. J. Heat and Fluid Flow* **17**, (3), pp. 245-254, 1996.
- [24] Craft, T. J., Developments in a low-Reynolds-number second-moment closure designed and its applications to separating and reattaching flows, *Int. J. Heat and Fluid Flow* **19**, (5), pp. 541-548, 1998.
- [25] Speziale, C.G., On nonlinear $k-\ell$ and $k-\varepsilon$ models of turbulence, *Journal of Fluid Mechanics*, **227**, pp. 247-272, 1987.
- [26] Shih, T. H., Zhu, J., and Lumley, J. L., A new Reynolds-stress algebraic equation model," *Computational Methods in Applied Mechanics*, **125**, pp. 287-302, 1995.
- [27] Patel, V. C., Chen, H. C., and Ju, S., "Solution of the fully-elliptic Reynolds-averaged Navier–Stokes equations and comparisons with experiments," IIHR Report No. 323, Iowa City, Iowa, 1988.
- [28] Patel, V. C., Rodi, W., and Scheuerer, G., Turbulence models for near-wall and low-Reynolds number flows: A review, *AIAA Journal*, **23**, pp. 1308-1319, 1985.
- [29] Wilcox, D.C., Simulation of transition with a two-equation turbulence model, *AIAA Journal*, **32**, (2), pp. 247-255, 1994.
- [30] Abid, R., Rumsey, C., and Gatski, T., Prediction of non-equilibrium turbulent flows with explicit algebraic stress models, *AIAA Journal*, **33**, (11), pp. 2026-2031, 1995.
- [31] Sofialidis, D., and Prinos, P., Wall suction effects on the structure of fully developed turbulent pipe flow, *ASME Journal of Fluids Engineering*, **118**, (1), pp. 33-39, 1996.
- [32] Menter, F.R., Zonal two equation $k-\omega$ turbulence models for aerodynamic flows, 24th AIAA Fluid Dynamics Conference, Orlando, Florida, pp. 1-21, 1993, July 6-9.
- [33] Neary, V. S., Sotiropoulos, F., and Odgaard, A. J., Three-dimensional numerical model of lateral-Intake flows, *ASCE Journal of Hydraulic Engineering*, **125**, (2), pp. 126-140, 1999.

- [34] Sotiropoulos, F., and Abdallah, S., A primitive variable method for the solution of three-dimensional incompressible viscous flows, *Journal of Computational Physics*, **103**, (2), pp. 336-349, 1992.
- [35] Sotiropoulos, F., and Patel, V. C., Flow in curved ducts of varying cross-section. Iowa Institute of Hydraulics Research (IIHR) Report No. 358, Univ. of Iowa, Iowa City, Iowa, July 1992.
- [36] Brandt, A., Multi-level adaptive solutions to boundary-value problems, *Mathematics of Computation*, **31**, (138), pp. 333-390, 1977.
- [37] Jameson, A., Multigrid algorithms for compressible flow calculations, MAE Report 1743, Princeton University, Princeton, NJ 08544, 1985.
- [38] Davis, D. O., and Gessner F. B., Experimental investigation of turbulent flow through a circular-to-rectangular transition duct, *AIAA Journal*, **30**, (2), pp. 367-375, 1992.
- [39] Larsson, L., Patel, V.C., and Dyne, G. (Eds.), Proceedings, 1990 SSPA-CTH-IIHR Workshop on Ship Viscous Flow, Flowtech International, Report No. 2, 1990.
- [40] Kodama, Y. (Ed.), Proceedings, CFD Workshop, Ship Research Institute, Tokyo, Japan, 1994.
- [41] Denker, J., Knaak, T., and Kux, J., Experiments and numerical investigation of the HSVA2 tanker (second test case of the 1990 SSPA-CTH-IIHR workshop), Institut für Schiffbau, University of Hamburg, Germany, Report No. 516, 1991.
- [42] Kim, W. J., and Patel, V. C., Origin and decay of longitudinal vortices developing in a curved rectangular duct, *ASME Journal of Fluids Engineering*, **116**, (1), pp. 45-51, 1994.
- [43] Bradshaw, P., Turbulent secondary flows, *Ann. Rev. Fluid Mech.*, **19**, pp. 53-74, 1987.
- [44] Patel, V. C., Perspective: Flow at high Reynolds number and over rough surfaces - Achilles heel of CFD, *ASME Journal of Fluids Engineering*, **120**, (3), pp. 434-444, 1998.